Journal of Quantitative Spectroscopy & Radiative Transfer 151 (2015) 97–109

Contents lists available at ScienceDirect

Journal of Quantitative Spectroscopy & Radiative Transfer

journal homepage: www.elsevier.com/locate/jqsrt

Effect of mineral dust aerosol aspect ratio on polarized reflectance

Xin Huang [a], Ping Yang [a,*], George Kattawar [b], Kuo-Nan Liou [c]

[a] Department of Atmospheric Sciences, Texas A&M University, College Station, TX 77843, USA
[b] Department of Physics & Astronomy, Texas A&M University, College Station, TX, USA
[c] Joint Institute for Earth System Science and Engineering, and Department of Atmospheric and Oceanic Sciences, University of California, Los Angeles, Los Angeles, CA, USA

ARTICLE INFO

Article history:
Received 21 May 2014
Received in revised form
9 September 2014
Accepted 11 September 2014
Available online 28 September 2014

Keywords:
Dust aerosol
Aspect ratio
Polarization measurement
Satellite

ABSTRACT

The effects of dust particle aspect ratios on single- and multiple-scattering processes are studied using the spheroidal model in order to obtain a better understanding of the radiance and polarization signals at the top of the atmosphere (TOA) under various dust-aerosol-loading conditions. Specifically, the impact of the particle aspect ratio on the polarization state of the TOA radiation field is demonstrated by comparing the normalized polarized radiances observed by the POLDER (POLarization and Directionality of the Earth's Reflectances) instrument on board the PARASOL (Polarisation et Anisotropie des Reflectances au sommet de l'Atmosphère, couples avec un Satellite d'Observation emportant un Lidar) satellite with the corresponding theoretical counterparts. Furthermore, presented are the aspect ratio values inferred from multi-angular polarized radiance measurements of Saharan and Asian dust by the POLDER/PARASOL.

1. Introduction

Atmospheric aerosol affects the radiation budget of the Earth–atmosphere system, both directly by a magnitude comparable to the radiative effect of greenhouse gases [1] and indirectly by acting as cloud nuclei [2]. Due to the significant spatial and temporal variations in its microphysical and chemical properties, aerosol has been recognized as a significant source of the uncertainties that afflict global climate models [3,4]. Mineral dust aerosol, originating from arid and semi-arid regions, contribute a major portion of atmospheric aerosol mass loading [5]. The estimated global annual mineral dust aerosol emission is between 1604 and 1960 Tg [6]. Depending on the particle size and influenced by gravitational settling, the atmospheric lifetime of mineral dust aerosol may vary from a few hours to several years [7]. After being lifted into the atmosphere, mineral dust aerosol may be transported thousands of miles by large-scale circulation and may affect both regional and global climate [2,6,7]. Quantification of the radiative effects of mineral dust aerosol requires global scale property measurements, which can be achieved only by satellite remote sensing.

Retrieval of the mineral dust aerosol properties from satellite measurements relies on our knowledge of dust particle single-scattering properties, including the single-scattering albedo, extinction coefficient, and scattering phase matrix [8,9]. Unfortunately, in laboratory measurements, the phase matrix can be obtained only at specific wavelengths and in limited angular scattering regions, for example, 3° to 177° [10], because experimentally measuring the forward and backward scattering is difficult to do in the visual region of the spectrum. Therefore, some important parameters, such as the asymmetry factor, cannot precisely be determined. Theoretical simulations of the scattering of light by

* Corresponding author.
E-mail address: pyang@tamu.edu (P. Yang).

http://dx.doi.org/10.1016/j.jqsrt.2014.09.014
0022-4073/

real dust particles are also impractical. From electron microscope imaging and energy-dispersive spectroscopy, dust particles are generally found to be irregular in shape and inhomogeneous in composition [11], which pose a pronounced challenge to the simulation of light scattering. Numerical techniques, such as the discrete-dipole approximation (DDA) [12,13], may be suitable for modeling complicated morphologies; however, in the visible spectral region, these methods are impractical for coarse mode dust particles with relatively large size parameters. The computational burden becomes even more severe when ensemble averaging over the particle size distribution and orientation is necessary for practical applications. The simple spherical mineral dust aerosol model, which has an exact theoretical solution based on the Lorenz–Mie theory, has been extensively used in aerosol property retrieval, but evidence has shown that the spherical shape assumption leads to substantial errors in retrieving aerosol optical thicknesses and in estimating the climate forcing effect of mineral dust aerosols [14–17]. To account for the non-sphericity of dust particles, the spheroidal model has been developed and has significantly improved aerosol property retrieval [18–20]. In the spheroidal model, the aspect ratio, defined as the ratio of the major axis to the minor axis of the spheroid, is introduced in addition to the particle size [21]. Special attention must be called to the fact that, even with modern parallel computation, obtaining the single-scattering properties of particles lacking an axis of symmetry is computationally costly. In practice, relatively simple morphologies are assumed to model the optical properties of dust particles. For example, a mineral dust aerosol database based on the ellipsoid model has been developed, which allows for fast retrieval of the single-scattering properties of randomly oriented polydisperse dust particles [22].

Although realistic dust particles may have far from spheroidal geometries and, indeed, the limitations of the spheroidal model have been recognized [23–25], the mean aspect ratio provides a good measure to quantify the particle non-sphericity and other complexities, which are essential to the estimation of dust forcing in the atmosphere [26]. In fact, dust particle models, which are completely different in terms of particle shape, are able to approximately reproduce the measured dust particle phase matrices [27,28]. Thus, a simpler spheroid-like model can be used and the detailed shape effect can be included through the use of the aspect ratio. Ground based measurements have also shown that the mean aspect ratio behavior is related to the relative humidity [29]; therefore, including this parameter in global aerosol retrieval is desirable.

The sensitivity of space-borne radiometric observations to dust particle shape has been examined in several studies. Substantial variations in dust aerosol microphysical properties, such as particle size, refractive index, and shape, may pose severe problems in aerosol retrieval from multispectral single-viewing-angle radiance measurements [30]. Observations from multi-angle radiometry, e.g., the Multi-angle Imaging SepctroRadiometer (MISR), have been found to relieve the problem and to distinguish different mineral dust types over dark water [31–33]. However, due to relatively bright surfaces that may diminish the signal from the mineral dust aerosol, the retrieval of particle shape information over land from space-borne observations has seldom been reported. Light scattered by atmospheric molecules and dust particles is strongly polarized and the angular features are sensitive to the dust microphysical properties; whereas, light scattered by land surfaces is weakly polarized and spectrally gray in the visible spectral range [34]. The combined multi-angular radiance and polarized radiance measurements have been suggested to be able to derive aerosol properties with sufficient accuracy to be used for long-term global climate research, even when the land surface properties are unknown [35].

We present a theoretical study of the sensitivity of multi-angular and polarization measurements by POLDER/PARASOL to the mean aspect ratio of dust aerosols. A vector radiative transfer code based on the adding-doubling principle is developed to simulate the transfer of polarized radiation in the atmosphere. The modeling results are compared with POLDER/PARASOL observations over dust aerosol source regions. Section 2 reports the single-scattering properties of ensemble averaged poly-disperse dust aerosols based on the spheroidal model. Section 3 describes the vector radiative transfer model. Section 4 presents a sensitivity study of polarized signals at the top of the atmosphere (TOA) to dust microphysical properties. Section 5 presents the mean aspect ratio values of Saharan and Asian dust aerosols inferred from the POLDER/PARASOL measurements. The conclusions of this study are found in Section 6.

2. Single-scattering properties of mineral dust aerosols

In order to cover a wide range of wavelengths, particle sizes, and aspect ratio values to derive the single-scattering properties of dust particles without incurring a tremendous computational burden, we employ an existing tri-axial ellipsoidal mineral dust aerosol database [15]. The development of the database combined the intrinsic merits of several light-scattering computational methods, including the Lorenz–Mie theory, the T-matrix method, the Amsterdam DDA (ADDA), and an improved geometric optics method (IGOM), in terms of their complimentary capabilities to compute the single-scattering properties over a rather broad parameter space. Furthermore, the database formatted the single-scattering properties of randomly oriented ellipsoidal particles, such as the extinction cross-sections, the single-scattering albedos, and the phase matrices, into a kernel form [36]. Through the pre-calculated kernels stored in the database, the ensemble averaged single-scattering properties of poly-dispersed ellipsoidal particles can be efficiently derived. In this study, we model dust particles as prolate spheroids only. As a test of the sensitivity of the single-scattering properties to the aspect ratio for both fine mode and coarse mode mineral dust aerosols, Fig. 1 illustrates the kernel elements related to the polarized phase function P_{12} at a visible wavelength of 670 nm. The results show that, for the fine mode particles, an increasing aspect ratio leads to a decrease in the polarization at side scattering angles. Note, the radii of the equivalent-volume spheres for the fine mode particles are smaller than the incident wavelength. For the coarse

mode case, where the particle radii are comparable to the visible spectrum wavelengths, the angular variations of the polarization state display an oscillation feature. Particles with smaller aspect ratios tend to display larger oscillations in the scattered light polarization state. However, the oscillations are largely averaged out and no pronounced effect is observable when the poly-disperse dust aerosol particle size distribution is considered.

The kernels stored in the database describe the single-scattering properties of individual dust particles, averaged over a very narrow size bin, at a fixed wavelength. Considering that atmospheric dust aerosols are poly-dispersed

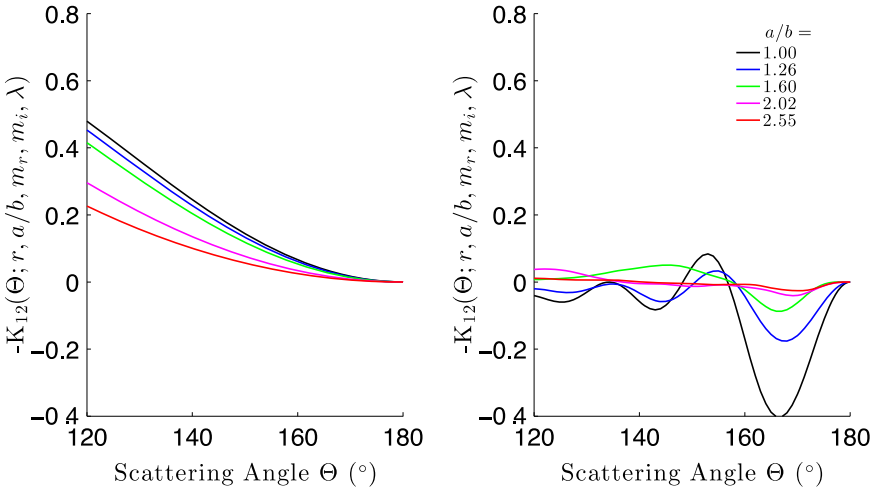

Fig. 1. Elements of kernel matrices $-\mathbf{K}_{12}(\Theta;r,a/b,m_r,m_i,\lambda)$ for different aspect ratios a/b, where the considered wavelength is 670 nm and the refractive index is set to be 1.53+0.0013i according to the AERONET observations for desert dust. The radii of the equivalent volume spheres at the centers of the bins are 0.1 μm (left panel) and 1.0 μm (right panel) to respectively represent fine mode and coarse mode particles.

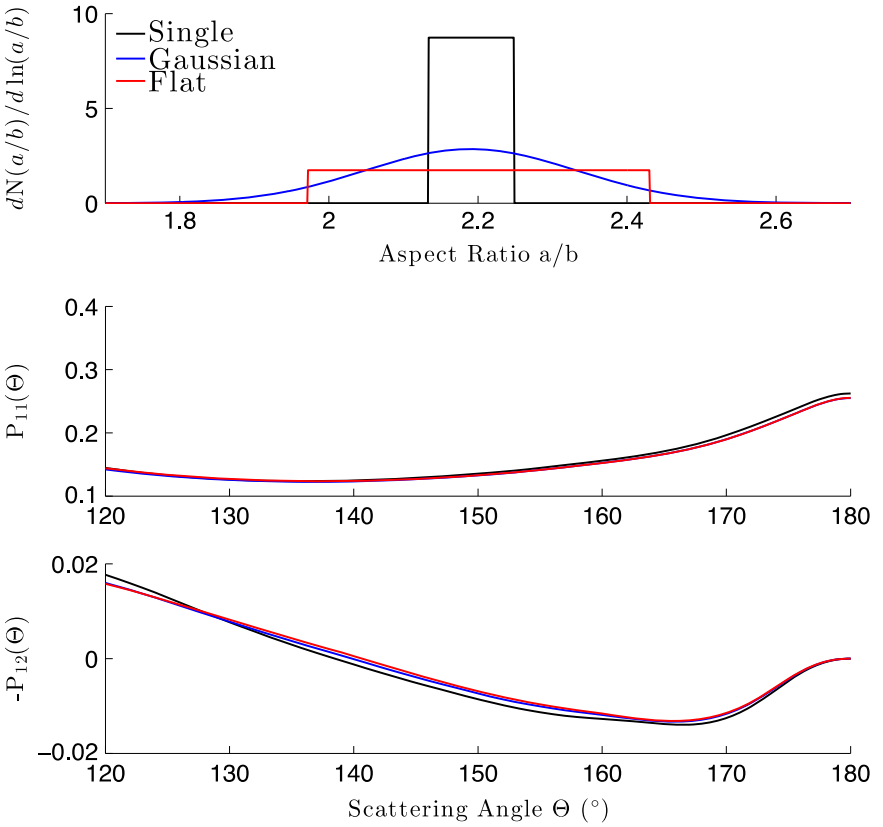

Fig. 2. Comparison of the phase functions and polarized phase functions of typical poly-dispersed dust particles with different aspect ratio distributions centered at the averaged aspect ratio: a delta function ("Single"), a Gaussian function ("Gaussian"), and a squared function ("Flat").

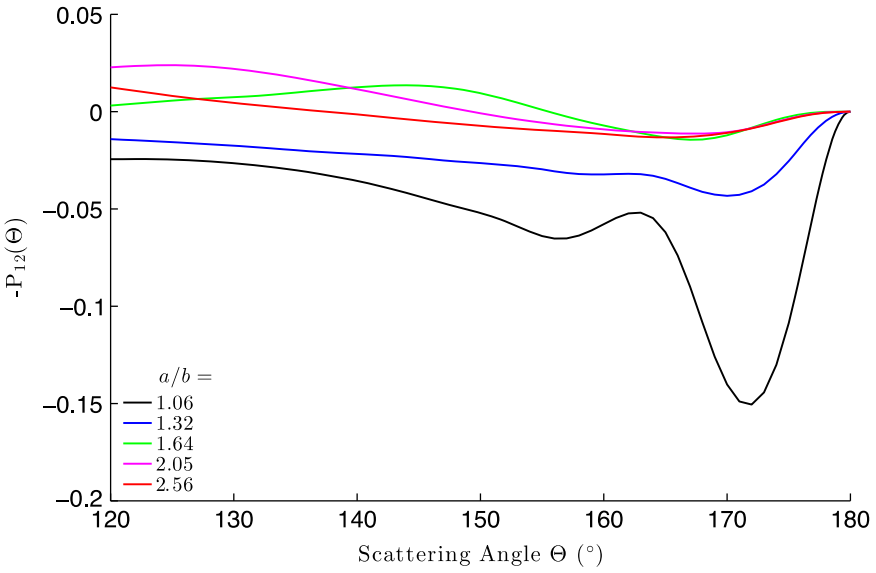

Fig. 3. Polarized phase functions of typical poly-dispersed dust particles with various averaged aspect ratios for the POLDER/PARASOL 670P band. The particle size distribution is assumed to be a bi-modal log-normal distribution and the parameters are taken from the AERONET desert dust measurements [51].

and the sensitivity of a satellite instrument as well as the solar spectrum may vary with respect to the wavelength within a spectral band of the instrument, the single-scattering properties over a particle size distribution $N(r)$ and the spectral band of the instrument must be averaged by considering the solar spectrum $S(\lambda)$ at the TOA and the instrumental response function $f(\lambda)$, where r is the radius of the equivalent-volume sphere (hereafter referred to as radius for simplicity), and λ is the wavelength. The narrow-band bulk scattering properties can be obtained in the form

$$\langle C_{\mathrm{ext/sca/abs}}(a/b)\rangle = \frac{\int_{\lambda_{\min}}^{\lambda_{\max}}\int_{\ln r_{\min}}^{\ln r_{\max}} C_{\mathrm{ext/sca/abs}}(r,a/b,m_r,m_i,\lambda)\frac{dN(r)}{d\ln r}f(\lambda)S(\lambda)d\ln r d\lambda}{\int_{\lambda_{\min}}^{\lambda_{\max}}\int_{\ln r_{\min}}^{\ln r_{\max}}\frac{dN(r)}{d\ln r}f(\lambda)S(\lambda)d\ln r d\lambda}, \tag{1}$$

$$\langle \mathbf{P}(\Theta;a/b)\rangle = \frac{\int_{\lambda_{\min}}^{\lambda_{\max}}\int_{\ln r_{\min}}^{\ln r_{\max}}\tilde{\mathbf{P}}(\Theta;r,a/b,m_r,m_i,\lambda)\frac{dN(r)}{d\ln r}f(\lambda)S(\lambda)d\ln r d\lambda}{\int_{\lambda_{\min}}^{\lambda_{\max}}\int_{\ln r_{\min}}^{\ln r_{\max}} C_{\mathrm{sca}}(r,a/b,m_r,m_i,\lambda)\frac{dN(r)}{d\ln r}f(\lambda)S(\lambda)d\ln r d\lambda}, \tag{2}$$

where $\tilde{\mathbf{P}}(\Theta;r,a/b,m_r,m_i,\lambda)$ is the un-normalized phase matrix defined as

$$\tilde{\mathbf{P}}(\Theta;r,a/b,m_r,m_i,\lambda) = C_{\mathrm{sca}}(r,a/b,m_r,m_i,\lambda)\mathbf{P}(\Theta;r,a/b,m_r,m_i,\lambda). \tag{3}$$

In Eqs. (1) and (2), the aspect ratio distribution variance with respect to the particle size is assumed to be uniform. For example, the particle size distribution can be separated from the corresponding particle shape (quantified in terms of the aspect ratio) distribution. Due to the smaller sizes of the fine mode particles compared with visible wavelengths, their aspect ratios are less important and, for simplicity, using the same aspect ratio distribution for both the fine and coarse modes is reasonable. Moreover, instead of considering the detailed aspect ratio distribution of dust particles [36], only the averaged aspect ratio is taken into account. The simplification is justified, as illustrated by Fig. 2, that the phase function and the polarized phase function of an ensemble of dust particles are relatively unaltered, at the backscattering angles of interest, as long as the averaged aspect ratio of the ensemble of dust particles is not changed, regardless of the details of the aspect ratio distribution.

Fig. 3 shows the typical narrowband bulk polarization properties of desert mineral dust aerosols with various averaged aspect ratios. The dominant mass loading of coarse mode dust particles in a desert region diminishes the polarization at side scattering angles. In comparison with the kernels of coarse mode dust particles, the polarization oscillations with the scattering angle are smoothed though the averaging process. Note that the negative peak around 170° for the near-spherical particle with an aspect ratio of 1.06 is preserved and can be used to distinguish non-spherical particles from quasi-spherical particles.

3. Radiative transfer model

To simulate the solar reflectance observed by a satellite sensor, we choose a multilayered plane-parallel atmosphere coupled with the surface. The multiple scattering due to dust aerosols and other atmospheric particles are fully considered by using a vector radiative transfer equation (VRTE). For a thin aerosol layer over ocean, the radiative transfer process is easily solved using only the first few order-of-scattering terms. The Fourier series expansion of the radiation field at the TOA converges rapidly for regularly shaped and small effective sized maritime absorbing aerosols. The ocean surface reflection can be considered with the well-tested Cox–Munk rough ocean surface model as a good approximation, and the reflected radiance is generally negligible outside the sun

glint region [37–39]. For optically thick aerosol layers over land, particularly over a dust aerosol source region, the corresponding radiative transfer simulation must incorporate much higher orders of scattering and thus requires significant computational time. Furthermore, because land surfaces are brighter and cannot be ignored for visible channels, complicated and diverse surface conditions are inevitable in the radiative transfer simulation. To address these issues, a rigorous radiative transfer model (hereafter referred to as the TAMU model) was developed based on the adding-doubling principle [40]. To optimize the TAMU model in terms of computational efficiency, many numerical techniques have been applied, such as, the separation of the first order scattering, the Delta-M/Delta-Fit truncation with the first order scattering correction [41,42], and the application of a linear algebra package for the supermatrix multiplications. Fig. 4 compares the computational efficiency of the TAMU model with one developed by de Haan et al. [40]. The evidence shows the TAMU model to be more efficient, particularly in cases involving coarse mode aerosols with large effective particle radii. For an effective particle radius of 6.3 μm, the computational accuracies of the two models are compared in Fig. 5 for an incident solar zenith angle of 60°. Overall, the relative discrepancies of the I component of the Stokes vector at the TOA are generally less than 0.02% with the maximum difference in the exact backward direction (e.g., viewing zenith angle −60°). The discrepancies of the Q component of the Stokes vector are usually less than 10^{-6}, which is an order of magnitude smaller than the absolute discrepancies of the I component, with the maximum difference in the horizontal direction. However, in this specific case, the TAMU model is more than 16 times faster.

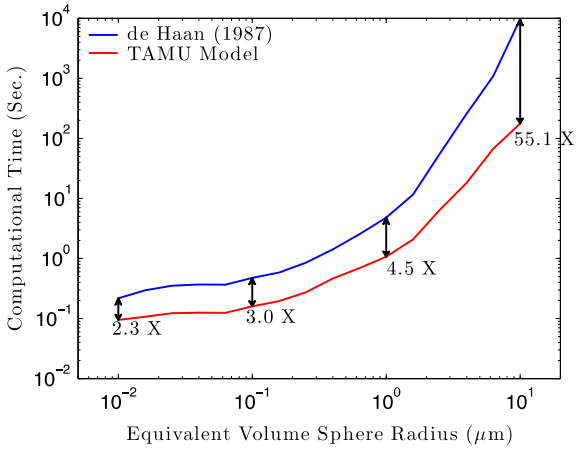

Fig. 4. Comparison of the computational time required between de Haan's model and the TAMU model for the calculation of the TOA reflectance at 670 nm of aerosol layers of optical depth 2 and with various particle sizes to reach the same precision (e.g., 10^{-6}) in the same computational condition. The number below each double arrow shows the ratio of the computation time of de Haan's model to that of the TAMU model for the specific size.

To account for the surface contribution to the TOA reflectance measurements, we consider the radiative transfer in a coupled atmosphere-surface system. The reflection properties of a surface can be described by a 4×4 bi-directional reflection distribution function (BRDF)

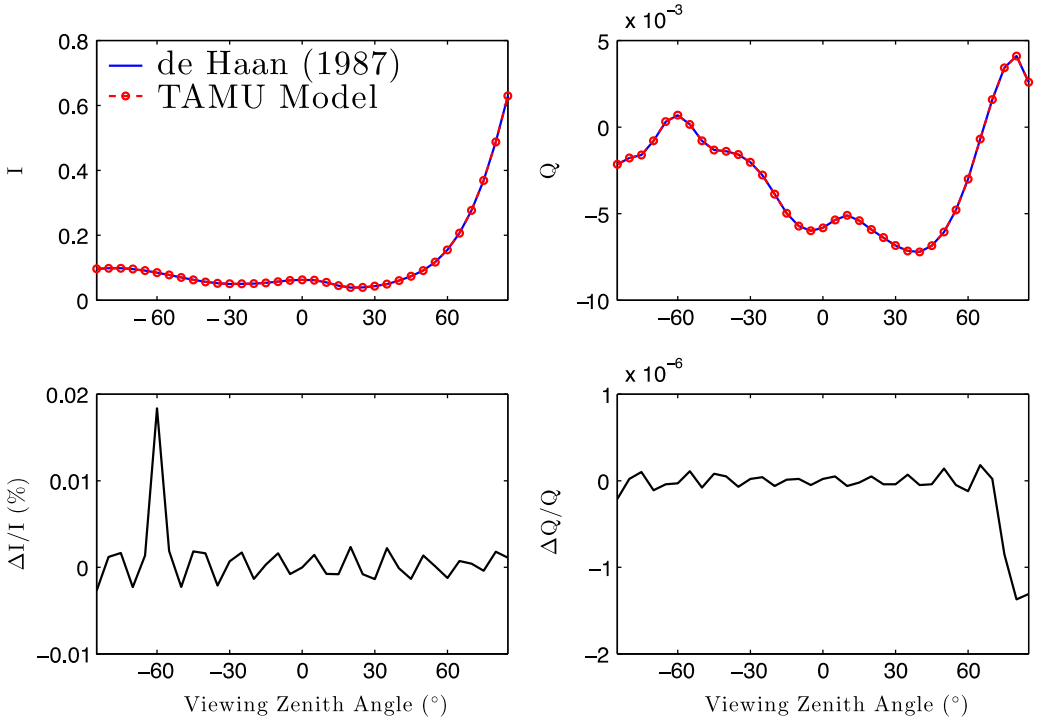

Fig. 5. Comparison between de Haan's code and the TAMU code of I and Q components of the reflected radiation at 670 nm by an aerosol layer of optical depth 2 with an effective particle radius 6.3 μm at the TOA and in the principal plane. The negative sign of the viewing zenith angle denotes that the azimuthal angle is 180°, while the positive value is for the 0° azimuthal angle. The incident solar zenith angle is assumed to be 60°.

matrix $\mathbf{R}_{\rm srf}$ as

$$\mathbf{I}(\mu,\varphi)=\frac{1}{\pi}\int_0^{2\pi}d\varphi'\int_0^1 d\mu'\mu'\mathbf{R}_{\rm srf}(\mu,\varphi;\mu',\varphi')\mathbf{I}_0(\mu',\varphi'), \tag{4}$$

where $\mathbf{I}_0(\mu,\varphi)$ is the Stokes vector of the radiation incident on the surface, and $\mathbf{I}(\mu,\varphi)$ is the Stokes vector of the radiation reflected by the surface. If no atmosphere is present and the solar flux $\mathbf{F}_0$ in direction (μ_0,φ_0) is directly incident on the surface, Eq. (4) becomes

$$\mathbf{I}(\mu,\varphi)=\frac{\mu_0}{\pi}\mathbf{R}_{\rm srf}(\mu,\varphi;\mu_0,\varphi_0)\mathbf{F}_0. \tag{5}$$

To fully consider the interaction between the atmosphere and the surface, the reflection matrix of the coupled atmosphere-surface system is calculated with the following adding equations:

$$\mathbf{Q}^{(1)}=\mathbf{R}^*_{\rm atm}\mathbf{R}_{\rm srf}, \tag{6}$$

$$\mathbf{Q}^{(p+1)}=\mathbf{Q}^{(1)}\mathbf{Q}^{(p)}, \tag{7}$$

$$\mathbf{Q}=\sum_{p=1}^{\infty}\mathbf{Q}^{(p)}, \tag{8}$$

$$\mathbf{D}=\mathbf{T}_{\rm atm}+\mathbf{Q}\mathbf{E}_{\rm atm}+\mathbf{Q}\mathbf{T}_{\rm atm}, \tag{9}$$

$$\mathbf{U}=\mathbf{R}_{\rm srf}\mathbf{E}_{\rm atm}+\mathbf{R}_{\rm srf}\mathbf{D}, \tag{10}$$

$$\mathbf{R}_{\rm atm+srf}=\mathbf{R}_{\rm atm}+\mathbf{E}_{\rm atm}\mathbf{U}+\mathbf{T}^*_{\downarrow}\mathbf{U}, \tag{11}$$

where $\mathbf{R}_{\rm atm}$ and $\mathbf{T}_{\rm atm}$, respectively, are 4×4 matrices representing the diffuse reflection and transmission properties of the atmosphere when light is incident on the top; $\mathbf{R}^*_{\rm atm}$ and $\mathbf{T}^*_{\rm atm}$ are the corresponding matrices for the case of light incident on the bottom; and, the 4×4 diagonal matrix $\mathbf{E}_{\rm atm}$ indicates the direct transmission of the atmosphere which is defined as

$$\mathbf{E}_{\rm atm}=\exp\left(-\frac{\tau_{\rm atm}}{\mu}\right)\mathbf{1}, \tag{12}$$

where τ_{atm} is the optical thickness of the atmosphere, μ is the absolute value of the cosine of the zenith angle of the incident beam, and $\mathbf{1}$ is the 4×4 identity matrix. Here, products among matrices differ from the usual matrix product but are defined as

$$\mathbf{AB}\equiv\frac{1}{\pi}\int_0^{2\pi}d\varphi''\int_0^1 d\mu''\mu''A(\mu,\mu'',\varphi-\varphi'')B(\mu'',\mu',\varphi''-\varphi'). \tag{13}$$

Numerically, evaluation of an integral such as the one in Eq. (13) is very time-consuming. By expanding each matrix in terms of the azimuthal angle into a Fourier series summation, integrations over the azimuthal angle can be reduced. If a matrix $\mathbf{A}(\mu,\mu',\varphi-\varphi')$ obeys the symmetry relation:

$$\mathbf{A}(\mu,\mu',\varphi-\varphi')=\Delta\mathbf{A}(\mu,\mu',\varphi'-\varphi)\Delta, \tag{14}$$

which is true if the particles in the scattering medium are randomly oriented and mirror-symmetric in the scattering plane, the matrix can be expanded as

$$\mathbf{A}(\mu,\mu',\varphi-\varphi')=\frac{1}{2}\sum_{m=0}^{\infty}(2-\delta_{m,0})\times\left[\Delta^{+m}(\varphi-\varphi')\mathbf{A}^m(\mu,\mu')(\mathbf{1}+\Delta)+\Delta^{-m}(\varphi-\varphi')\mathbf{A}^m(\mu,\mu')(\mathbf{1}-\Delta)\right], \tag{15}$$

where

$$\Delta=\mathrm{diag}(1,1,-1,-1), \tag{16}$$

$$\Delta^{+m}(\varphi)=\mathrm{diag}(\cos m\varphi,\ \cos m\varphi,\ \sin m\varphi,\ \sin m\varphi), \tag{17}$$

$$\Delta^{-m}(\varphi)=\mathrm{diag}(-\sin m\varphi,-\sin m\varphi,\ \cos m\varphi,\ \cos m\varphi), \tag{18}$$

and the m-th Fourier component is given by

$$\mathbf{A}^m(\mu,\mu')=\frac{1}{2\pi}\int_0^{2\pi}d(\varphi-\varphi')\left[\Delta^{+m}(\varphi-\varphi')+\Delta^{-m}(\varphi-\varphi')\right]\mathbf{A}(\mu,\mu',\varphi-\varphi'). \tag{19}$$

For the m-th Fourier component, Eqs. (6)–(11) hold by adding the superscript m and expressing the product as

$$\mathbf{A}^m\mathbf{B}^m\equiv2\int_0^1 d\mu''\mu''\mathbf{A}^m(\mu,\mu'')\mathbf{B}^m(\mu'',\mu'), \tag{20}$$

which can be computed following the super-matrix formalism suggested by de Haan et al. [40]. To optimize the computational efficiency, the first order scattering contribution is separated in the calculation to accelerate the convergence of the Fourier series. For example,

$$\mathbf{R}_{\rm atm+srf}(\mu,\mu',\varphi-\varphi')=\mathbf{R}^{(1)}_{\rm atm+srf}(\mu,\mu',\varphi-\varphi')+\frac{1}{2}\sum_{m=0}^{\infty}(2-\delta_{m,0})\times\left\{\Delta^{+m}(\varphi-\varphi')\left[\mathbf{R}^m_{\rm atm+srf}(\mu,\mu')-\mathbf{R}^{(1)m}_{\rm atm+srf}(\mu,\mu')\right](\mathbf{1}+\Delta)+\Delta^{-m}(\varphi-\varphi')\left[\mathbf{R}^m_{\rm atm+srf}(\mu,\mu')-\mathbf{R}^{(1)m}_{\rm atm+srf}(\mu,\mu')\right](\mathbf{1}-\Delta)\right\} \tag{21}$$

where

$$\mathbf{R}^{(1)}_{\rm atm+srf}(\mu,\mu',\varphi-\varphi')=\mathbf{R}^{(1)}_{\rm atm}(\mu,\mu',\varphi-\varphi')+\exp\left(-\frac{\tau_{\rm atm}}{\mu}-\frac{\tau_{\rm atm}}{\mu'}\right)\mathbf{R}_{\rm srf}(\mu,\mu',\varphi-\varphi'), \tag{22}$$

$$\mathbf{R}^{(1)m}_{\rm atm+srf}(\mu,\mu')=\mathbf{R}^{(1)m}_{\rm atm}(\mu,\mu')+\exp\left(-\frac{\tau_{\rm atm}}{\mu}-\frac{\tau_{\rm atm}}{\mu'}\right)\mathbf{R}^m_{\rm srf}(\mu,\mu'). \tag{23}$$

The surface BRDF in this work is adapted from the parameterization of Liou et al. [43] based on the reflectance of a vegetated surface and a sand surface measured by Suomalainen and Peltoniemi [44]. Both bidirectional reflectance and degree of the linear polarization measurements are considered to account for the polarized anisotropic features of the land surface. The parameterized surface BRDF model can be expressed as

$$\mathbf{R}_{\rm srf}(\mu,\mu_0,\varphi-\varphi_0)=\begin{pmatrix}A & A_{12} & 0 & 0\\ A_{12} & A & 0 & 0\\ 0 & 0 & 0 & 0\\ 0 & 0 & 0 & 0\end{pmatrix}, \tag{24}$$

where A is a constant and A_{12} is in the form of:

$$A_{12}=-C\frac{\cos^{-1}\mu}{\pi}\cos(\varphi-\varphi_0) \tag{25}$$

with a constant parameter C to distinguish different surface polarization scenarios.

For the visible channels of the POLDER/PARASOL, the absorption and Rayleigh scattering from atmospheric molecules are small but cannot be ignored. In spite of the small optical thicknesses, the contribution of the molecular Rayleigh scattering to the polarized radiance measurements is significant due to strongly polarized scattered light in side-scattering directions when the wavelength is considerably larger than the sizes of gas molecules. The effects are exactly taken into account with the line-by-line radiative transfer model (LBLRTM) [45], where the high-spectral-resolution molecular absorption and Rayleigh scattering optical thicknesses are calculated from the standard atmospheric profiles by considering up to 39 major atmospheric gases based on spectral lines from the HITRAN database [46]. The narrow band optical depth for a particular channel of the POLDER/PARASOL can be approximately obtained by integrating the high-spectral-resolution transmittance weighted by the response function $f(\lambda)$ of the channel:

$$\overline{\tau}_{\text{Rayleigh/absorption}} = -\log\left(\frac{\int_{\lambda_{\min}}^{\lambda_{\max}} \exp(-\tau_{\text{Rayleigh/absorption}}(\lambda) f(\lambda) d\lambda)}{\int_{\lambda_{\min}}^{\lambda_{\max}} f(\lambda) d\lambda}\right), \tag{26}$$

where $\lambda_{\min}$ and $\lambda_{\max}$ are the lower and upper limits of the band wavelengths.

4. Sensitivity study

For a clear pixel, the multi-angular radiance and polarized radiance measurements at the TOA are affected by the surface BRDF, aerosol optical thickness, and the single-scattering properties fundamentally determined by aerosol particle size, aerosol complex refractive index, and the particle aspect ratio. However, the methods in which these factors affect the measurements are distinct.

As is shown in Fig. 6, both the radiance (I) and the degree of linear polarization ($-Q/I$) at the TOA are sensitive to variations in aerosol optical thickness. When the aerosol optical thickness increases, the radiance I at the TOA increases which is contrary to the magnitude of the angular variations of the $-Q/I$ values. The explanation is that multiple scattering tends to enhance the intensity of the backscattering, but to diminish the polarization feature of the reflected light. However, the effect is no longer present when the optical thickness becomes so large that the corresponding radiative transfer process enters into the diffuse region, where both the radiance and the degree of linear polarization approach their asymptotic values [47].

The effects of aerosol particle size on the radiation at the TOA are presented in Figs. 7 and 8. The radiance I shows little sensitivity to the particle size around the nadir viewing direction (e.g., the viewing zenith angle range from -30° to 30°), compared to the quantity $-Q/I$. As the aerosol particle size increases, the value of $-Q/I$ generally decreases in both the fine mode and coarse mode cases. When the median particle radius of the fine mode aerosols decreases, $-Q/I$ becomes less positive for the viewing zenith angle range from -30° to 0°, as illustrated in the right panel of Fig. 7. When the median particle radius of the coarse mode aerosols decreases, $-Q/I$ becomes more negative for the viewing zenith angle range from 0° to 30°, as evident from the right panel of Fig. 8.

Fig. 9 illustrates the influence of the real part of the refractive index of mineral dust aerosols on the TOA radiance and polarized radiance measurements. While there is a slight decrease in the I component when the particle becomes optically softer, that is, the real part of the refractive index becomes smaller, the value of $-Q/I$ significantly increases in the viewing zenith angle range from -30° to 0°. The corresponding sensitivity studies for the imaginary part of the refractive index were not carried out, because mineral dust aerosols, particularly aerosols over a desert region, are usually so weakly absorbing in the visible spectrum that the typical value of the imaginary part of the refractive index is too small to induce a pronounced effect on radiometric measurements.

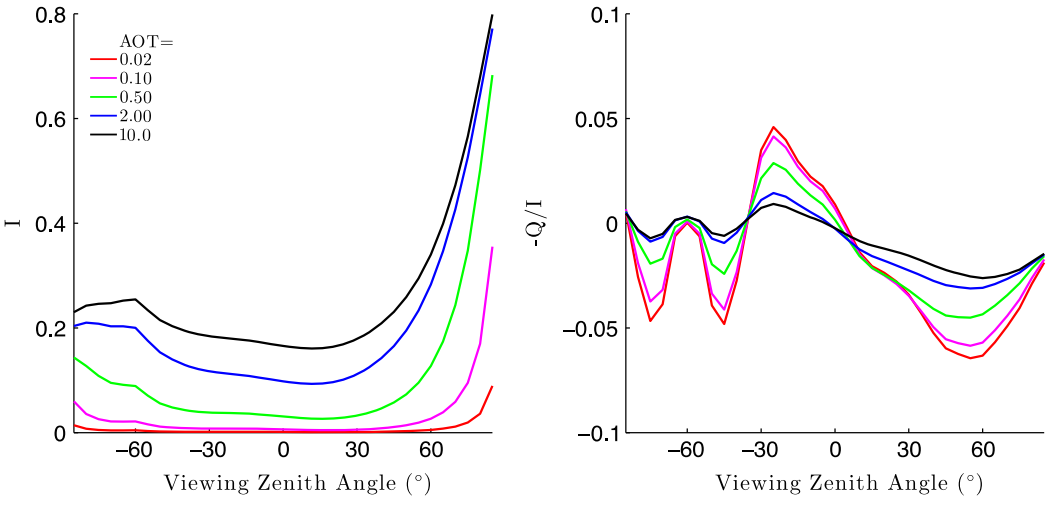

Fig. 6. Influence of the aerosol optical thickness on radiance and degree of linear polarization at the TOA and in the principal plane when the incident solar zenith angle is 60°. The aerosol model is the bi-modal spheroidal model based on the AERONET retrieval results.

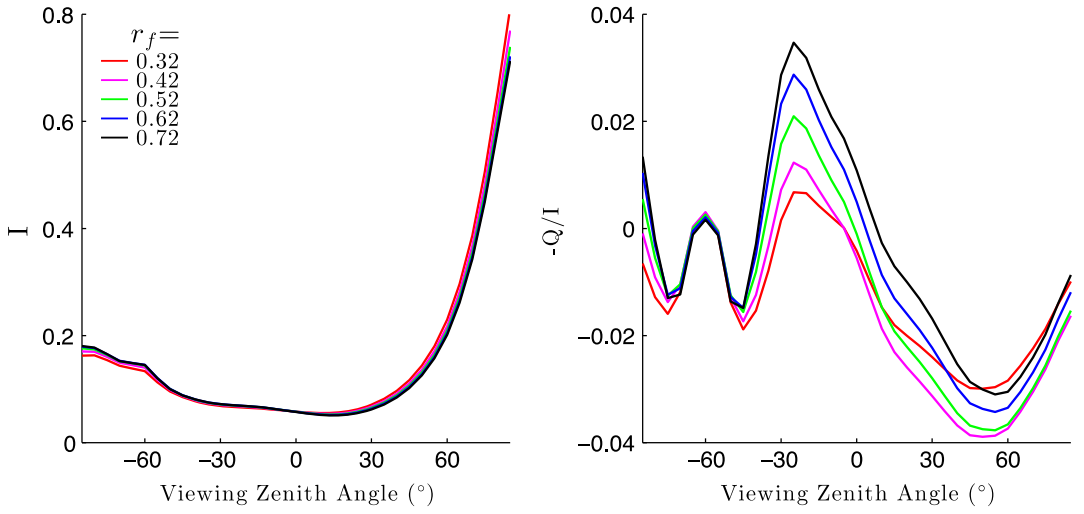

Fig. 7. Influence of the median particle radius of fine mode aerosols on radiance and the degree of linear polarization at the TOA and in the principal plane when the incident solar zenith angle is 60°. The aerosol optical thickness is assumed to be 0.5 and the aerosol model is the bi-modal spheroidal model based on the AERONET retrieval results.

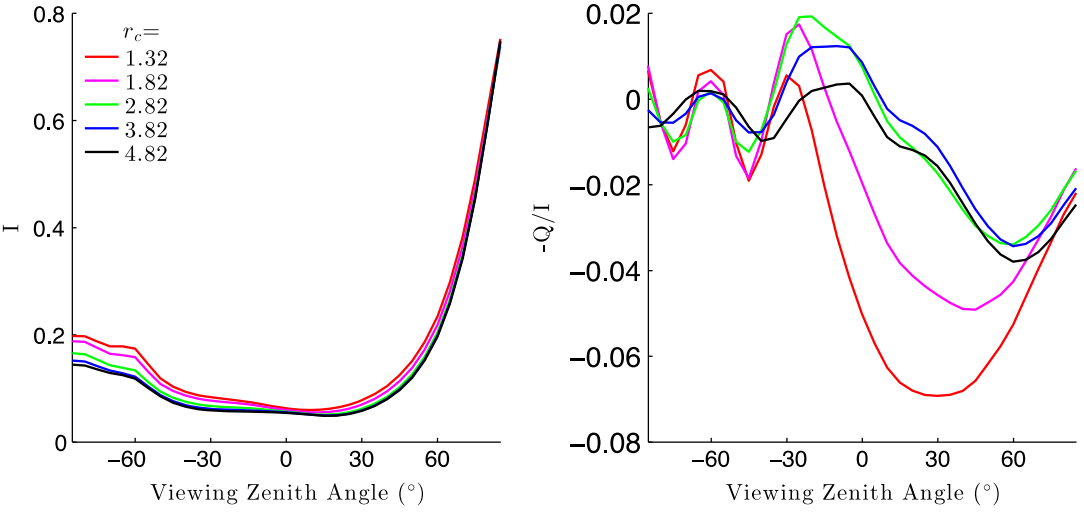

Fig. 8. Influence of the median particle radius of coarse mode aerosols on radiance and the degree of linear polarization at the TOA and in the principal plane when the incident solar zenith angle is 60°. The aerosol optical thickness is assumed to be 0.5 and the aerosol model is the bi-modal spheroidal model based on the AERONET retrieval results.

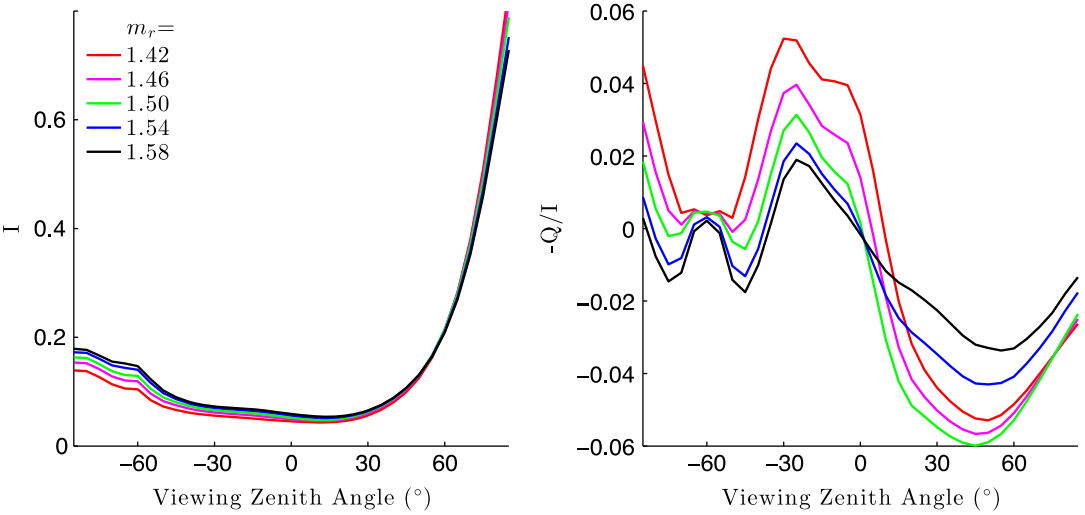

Fig. 9. Influence of the real part of the refractive index of mineral dust aerosols on radiance and the degree of linear polarization at the TOA and in the principal plane when the incident solar zenith angle is 60°. The aerosol optical thickness is assumed to be 0.5 and the aerosol model is the bi-modal spheroidal model based on the AERONET retrieval results.

As shown in Fig. 10, both the radiance and the degree of linear polarization are sensitive to aspect ratio variations, but in different angular regions and in different ways. At angles around the exact backscattering direction (e.g., the scattering angle range from 180° to 150° corresponding to the viewing zenith angle range from −60° to −30°), the radiance I decreases as the aspect ratio increases from unity; and, at side-scattering angles (e.g., the scattering angle range from 120° to 60° corresponding to the viewing zenith angle range from 0° to 60°), the $-Q/I$ changes from negative to positive when the particles change from quasi-spherical to non-spherical.

Given the land surface BRDF model described in the previous section, the land surface properties are parameterized by factors A and C in Eqs. (24) and (25), which respectively represent the reflection and polarization properties

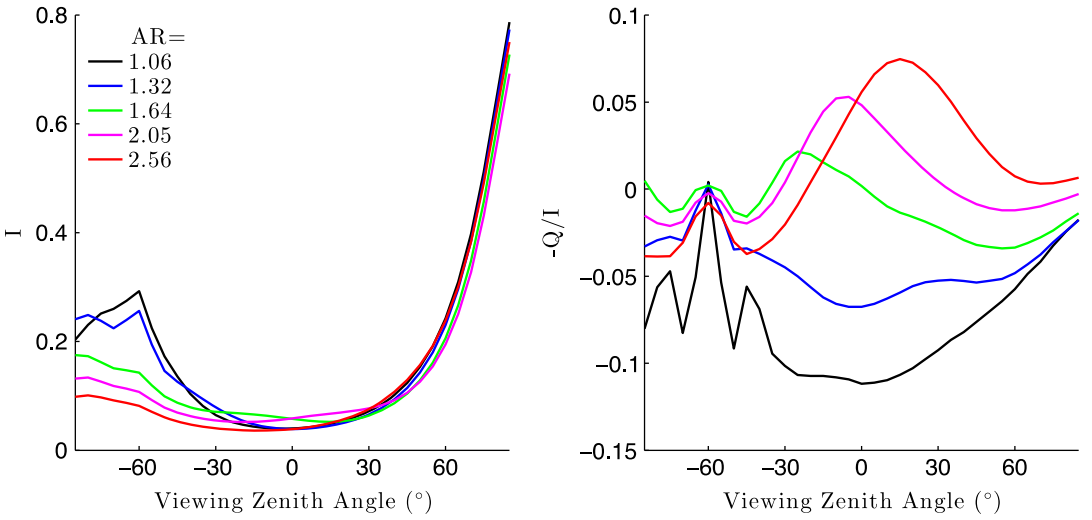

Fig. 10. Influence of the mineral dust aerosol aspect ratio on radiance and the degree of linear polarization at the TOA and in the principal plane when the incident solar zenith angle is 60°. The aerosol optical thickness is assumed to be 0.5 and the aerosol model is the bi-modal spheroidal model based on the AERONET retrieval results.

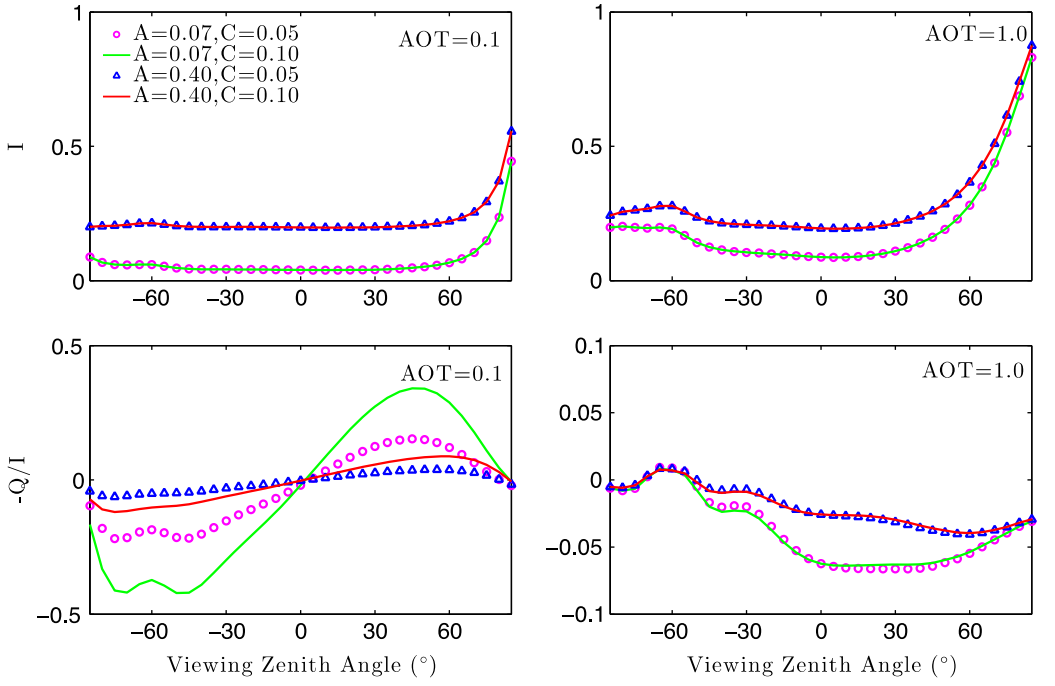

Fig. 11. Influence of land surface properties on the radiance and the degree of linear polarization at the TOA and in the principal plane when the incident solar zenith angle is 60°. The left two figures are for an optically thin aerosol layer scenario with aerosol optical thickness 0.1, while the right two figures are for an optically thick aerosol layer scenario with optical thickness 1.0. The aerosol model is the bi-modal spheroidal model based on the AERONET retrieval results.

of the land surface. Without an atmosphere above the land surface, the physical meaning of A and C can be simply interpreted as the surface albedo and the maximum degree of linear polarization of the surface. For example, $A=0.07$ represents a dark land surface, such as a vegetated ground, and $A=0.40$ represents a bright land surface, such as a sand ground; $C=0.05$ represents a neutral polarization land surface, while $C=0.10$ represents a land surface with some polarization features. As is shown in Fig. 11, the radiance measurements at the TOA are sensitive to the surface reflection A but not to the polarization surface C regardless of the optical thickness of the aerosol layer above the land surface. The explanation is that the Q component of natural light in the atmosphere is usually 1 or 2 orders of magnitude smaller than the I component. However, when an optically thin aerosol layer exists above the land surface, the degree of linear polarization shows a strong dependence on the polarization of the land surface; however, the degree of linear polarization is insensitive to the polarization properties of the land surface when the optical thickness of the aerosol layer is as large as 1.0. The TOA polarized radiance measurements are only sensitive to the scattering properties of the top portion of an optically thick scattering medium.

5. Dust particle aspect ratio inferred from space-borne polarized radiance measurements

The multi-angular radiance and polarized radiance measurements from the POLDER/PARASOL provide an unprecedented opportunity to study the aspect ratio of mineral dust aerosols. Launched in December 2004, the POLDER on board the PARASOL satellite is an orbiting instrument that provides radiance measurements at nine bands (443, 490, 565, 670, 763, 765, 865, 910, and 1020 nm) and linear polarization measurements at three bands (490, 670, and 865 nm) in up to 16 directions per pixel with a moderate nadir resolution of 6 km × 7 km [48]. The multi-angular normalized radiances $L(\theta_s,\theta_v,\phi)$ and polarized radiances $L_p(\theta_v,\theta_s,\phi)$ in the POLDER/PARASOL level 2 Earth Radiation Budget, Water Vapor, and Cloud products are considered in this study. The definition of $L(\theta_s,\theta_v,\phi)$ and $L_p(\theta_v,\theta_s,\phi)$ are given by

$$L(\theta_s,\theta_v,\phi)\equiv\frac{\pi I}{F_0} \tag{27}$$

$$L_p(\theta_v,\theta_s,\phi)\equiv \mathrm{sgn}\frac{\pi\sqrt{Q^2+U^2}}{F_0}\frac{\cos\theta_s+\cos\theta_v}{\cos\theta_s}, \tag{28}$$

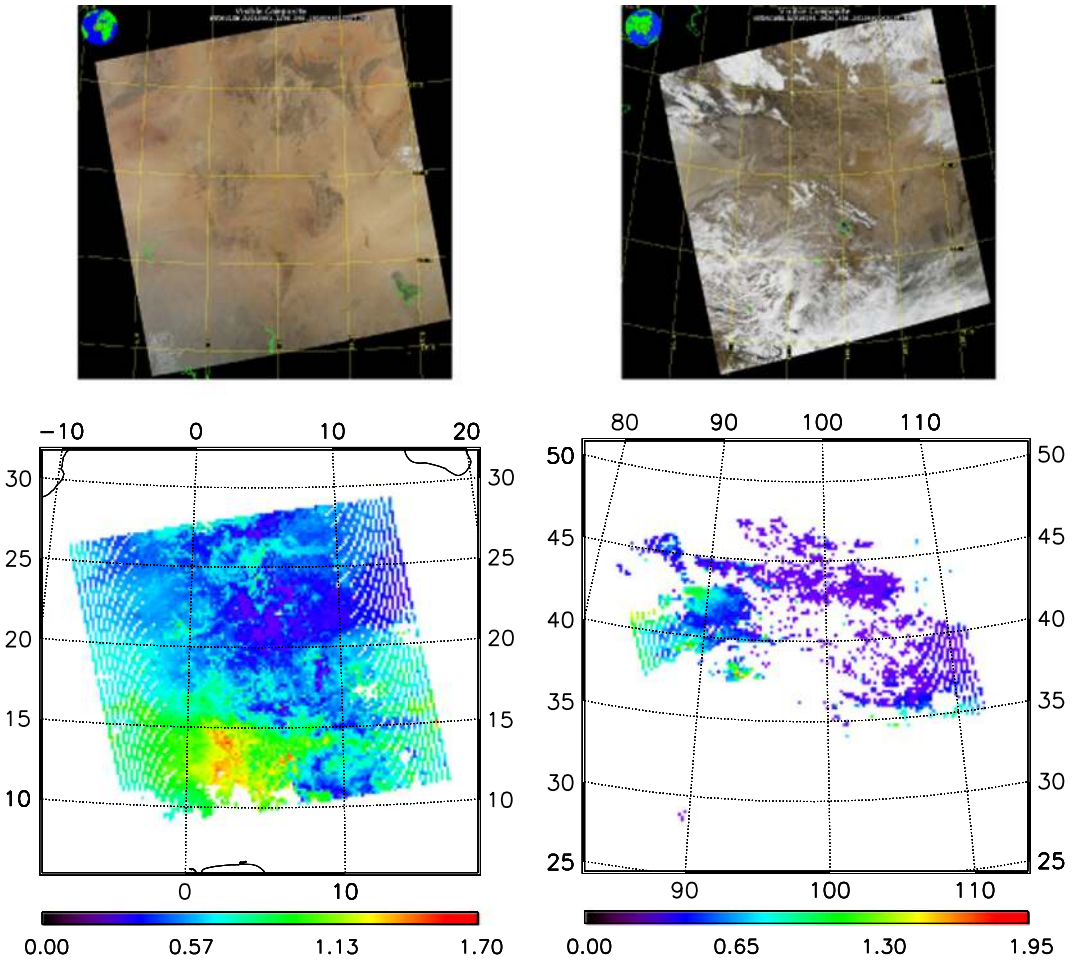

Fig. 12. The top two figures are the MODIS/Aqua RGB images for the Sahara Desert (left) and Northwest China (right) on April 1, 2010. The lower two figures are the corresponding aerosol optical thickness distributions retrieved using the MODIS Deep Blue aerosol retrieval algorithm.

where θ_v is the viewing zenith angle, θ_s is the solar zenith angle, ϕ is the relative azimuthal angle between the solar and viewing directions, F_0 is the incident solar flux at the TOA, and the sign (sgn) of $L_p(\theta_v, \theta_s, \phi)$ is determined by the angle between the direction of the polarization and the normal direction of the scattering plane [49]. If twice the angle is either in the first or the fourth quadrant, the sign is positive; otherwise, the sign is negative.

To exclude the land surface influence and the effect due to a variance in aerosol optical thickness, only dusty pixels covered with optically thick aerosol layers are considered. Because the highly reflective land surface in the visible spectrum may blur the satellite signal associated with the dust aerosols, dusty pixel detection is achieved using the MODIS Deep Blue aerosol product, which takes advantage of the fact that the land surface becomes darker in the MODIS Deep Blue channels due to the relatively strong absorption of the dust aerosols in the near UV spectrum [50]. A comparison of MODIS RGB images and the distribution of the corresponding aerosol optical thicknesses at 675 nm derived in the MODIS Deep Blue product is shown in Fig. 12. The left two figures are for the Sahara Desert on April 1, 2010, where a strong dust storm can be observed around 2°East and 12°North. The right two figures are for Northwest China on the same day, where the Taklimakan Desert and the Gobi Desert, believed to be the sources of Asian dust aerosols, can be identified in the granule.

The dusty pixels detected by MODIS/Aqua are spatially and temporally collocated with POLDER/PARASOL to obtain the multi-angular radiance and polarized radiance measurements. The Sahara Desert results corresponding to the left panel of Fig. 12 are shown in Figs. 13 and 14, where radiance and polarized radiance measurements for dusty pixels with optical thicknesses larger than 0.8 are plotted. Since the surface reflectances as well as the aerosol optical thicknesses may vary significantly among the dusty pixels, the measured normalized radiance seems completely random over the scattering angle range; nevertheless, the measured normalized polarized radiance shows a strong angular dependence.

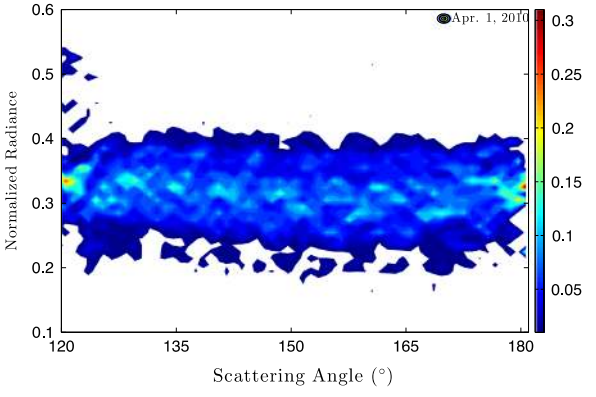

Fig. 13. Angular distribution of normalized radiance measured by POLDER/PARASOL on April 1, 2010 over the Sahara Desert. The color coding represents the probability to obtain a certain measurement at a particular scattering angle. (For interpretation of the references to color in this figure legend, the reader is referred to the web version of this article.)

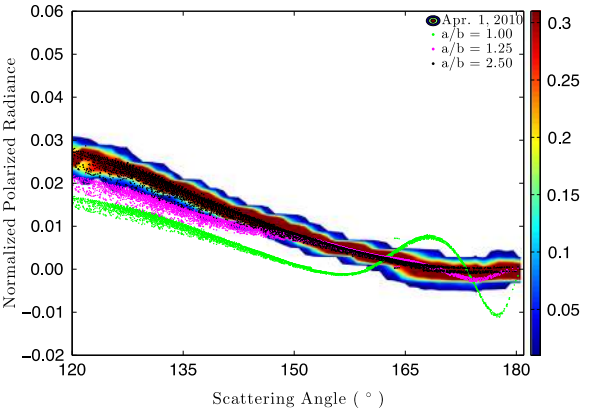

Fig. 14. Angular distribution of normalized polarized radiance measured by POLDER/PARASOL on April 1, 2010 over the Sahara Desert, compared with simulations using mineral dust aerosol models of various aspect ratios. The color coding represents the probability to obtain a certain measurement at a particular scattering angle. (For interpretation of the references to color in this figure legend, the reader is referred to the web version of this article.)

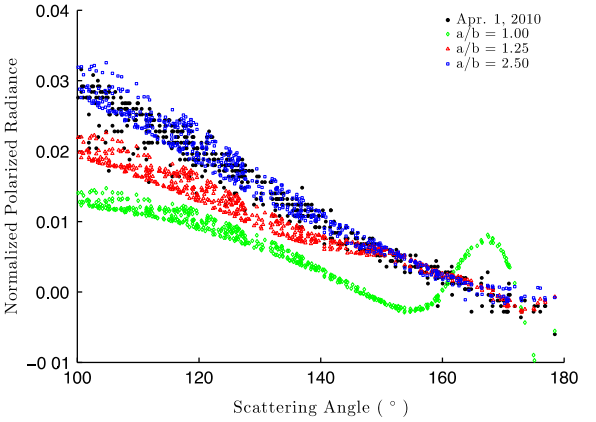

Fig. 15. Angular distribution of normalized polarized radiance measured by POLDER/PARASOL on April 1, 2010 over Northwest China, compared with simulations using mineral dust aerosol models of various aspect ratios.

Moreover, such an angular dependence can be well fit by simulations using the dust aerosol model with a mean aspect ratio of 2.5.

The multi-angular normalized polarized radiance for Northwest China observed by POLDER and corresponding to the right panel of Fig. 12 is shown in Fig. 15. The normalized polarized radiance diverges into two branches: one is the same as the Sahara case which can use the dust aerosol model with a mean aspect ratio of 2.5; the other, unlike the Sahara scenario, can be simulated by the dust aerosol model with a mean aspect ratio of 1.25.

6. Conclusions

We study the sensitivity of the multi-angular radiance and polarized radiance measurements made by POLDER/PARASOL to the aspect ratio of dust aerosols by using the

spheroidal model. Specifically, we employ a database of the single-scattering properties of mineral dust particles and a vector radiative transfer model to investigate, in detail, the sensitivity of multi-angular radiance and polarized radiance measurements to the dust aerosol properties and the land surface properties. From the collocated MODIS Deep Blue product and the PARASOL level 2 Earth Radiation Budget, Water Vapor, and Clouds product, the aspect ratios of Saharan and Asian dust are inferred. The radiation effect of Saharan dust is closely reproduced by the spheroidal aerosol model with a mean aspect ratio of 2.5, but Asian dust exhibits two branches, which correspond to mean aspect ratio values of 1.25 and 2.5.

Acknowledgment

This study was partly supported by a NASA grant (NNX11AK39G) and the endowment funds (02-512231-10000) related to the David Bullock Harris Chair in Geosciences at the College of Geosciences, Texas A&M University. Kattawar's research is partially supported by the ONR MURI program N00014-09-1-1054, and ONR N00014-11-1-0154, NSF Grant OCE 1130906.

References

[1] Charlson RJ, Langner J, Rodhe H, Leovy CB, Warren SG. Perturbation of the northern hemisphere radiative balance by backscattering from anthropogenic sulfate aerosols. Tellus A 1991;43:152–63.
[2] Lohmann U, Feichter J. Global indirect aerosol effects: a review. Atmos Chem Phys 2005;5:715–37.
[3] Sokolik IN, Winker DM, Bergametti G, Gillette DA, Carmichael G, Kaufman YJ, et al. Introduction to special section: outstanding problems in quantifying the radiative impacts of mineral dust. J Geophys Res 2001;106:18015–27.
[4] McCarthy JJ, Canziani OF, Leary NA, Dokken DJ, White KS, editors. Climate change 2001: impacts, adaptation, and vulnerability: contribution of Working Group II to the third assessment report of the Intergovernmental Panel on Climate Change. New York: Cambridge University Press; 2001.
[5] Chiapello I, Bergametti G, Chatenet B, Dulac F, Jankowiak I, Liousse C, et al. Contribution of the different aerosol species to the aerosol mass load and optical depth over the northeastern tropical Atlantic. J Geophys Res 1999;104:4025–35.
[6] Ginoux P, Chin M, Tegen I, Prospero JM, Holben B, Dubovik O, et al. Sources and distributions of dust aerosols simulated with the GOCART model. J Geophys Res 2001;106:20255–73.
[7] Tegen I, Fung I. Modeling of mineral dust in the atmosphere: sources, transport, and optical thickness. J Geophys Res 1994;99:22897–914.
[8] Gordon HR, Wang M. Retrieval of water-leaving radiance and aerosol optical thickness over the oceans with SeaWiFS: a preliminary algorithm. Appl Opt 1994;33:443–52.
[9] Mishchenko MI, Travis LD, Lacis AA. Scattering, absorption, and emission of light by small particles. Cambridge, UK: Cambridge University Press; 2002.
[10] Dabrowska DD, Muñoz O, Moreno F, Nousiainen T, Zubko E, Marra AC. Experimental and simulated scattering matrices of small calcite particles at 647 nm. J Quant Spectrosc Radiat Transf 2013;124:62–78.
[11] Nousiainen T, Zubko E, Niemi JV, Kupiainen K, Lehtinen M, Muinonen K, et al. Single-scattering modeling of thin, birefringent mineral-dust flakes using the discrete-dipole approximation. J Geophys Res 2009;114:D07207.
[12] Draine BT, Flatau PJ. Discrete-dipole approximation for scattering calculations. J Opt Soc Am A 1994;11:1491–9.
[13] Kalashnikova OV, Sokolik IN. Importance of shapes and compositions of wind-blown dust particles for remote sensing at solar wavelengths. Geophys Res Lett 2002;29:1398.
[14] Mishchenko MI, Lacis AA, Carlson BE, Travis LD. Nonsphericity of dust-like tropospheric aerosols: implications for aerosol remote sensing and climate modeling. Geophys Res Lett 1995;22:1077–80.
[15] Zhao TXP. A study of the effect of non-spherical dust particles on the AVHRR aerosol optical thickness retrievals. Geophys Res Lett 2003;30:1317.
[16] Kahnert M, Nousiainen T, Räisänen P. Mie simulations as an error source in mineral aerosol radiative forcing calculations. Q J R Meteorol Soc 2007;133:299–307.
[17] Mishchenko MI, Geogdzhayev IV, Liu L, Ogren JA, Lacis AA, Rossow WB, et al. Aerosol retrievals from AVHRR radiances: effects of particle nonsphericity and absorption and an updated long-term global climatology of aerosol properties. J Quant Spectrosc Radiat Transf 2003;79–80:953–72.
[18] Dubovik O, Holben BN, Lapyonok T, Sinyuk A, Mishchenko MI, Yang P, et al. Non-spherical aerosol retrieval method employing light scattering by spheroids. Geophys Res Lett 2002;29:1415.
[19] Wang J. The effects of non-sphericity on geostationary satellite retrievals of dust aerosols. Geophys Res Lett 2003;30:2293.
[20] Mishchenko MI, Travis LD, Kahn RA, West RA. Modeling phase functions for dustlike tropospheric aerosols using a shape mixture of randomly oriented polydisperse spheroids. J Geophys Res 1997;102:16831–47.
[21] Mishchenko MI, Travis LD. Light scattering by polydispersions of randomly oriented spheroids with sizes comparable to wavelengths of observation. Appl Opt 1994;33:7206–25.
[22] Meng Z, Yang P, Kattawar GW, Bi L, Liou KN, Laszlo I. Single-scattering properties of tri-axial ellipsoidal mineral dust aerosols: a database for application to radiative transfer calculations. J Aerosol Sci 2010;41:501–12.
[23] Kahnert FM, Stamnes JJ, Stamnes K. Can simple particle shapes be used to model scalar optical properties of an ensemble of wavelength-sized particles with complex shapes? J Opt Soc Am A 2002;19:521–31.
[24] Kalashnikova OV, Sokolik IN. Modeling the radiative properties of nonspherical soil-derived mineral aerosols. J Quant Spectrosc Radiat Transf 2004;87:137–66.
[25] Nousiainen T, Kahnert M, Lindqvist H. Can particle shape information be retrieved from light-scattering observations using spheroidal model particles? J Quant Spectrosc Radiat Transf 2011;112:2213–25.
[26] Colarco PR, Nowottnick EP, Randles CA, Yi B, Yang P, Kim K-M, et al. Impact of radiatively interactive dust aerosols in the NASA GEOS-5 climate model: sensitivity to dust particle shape and refractive index. J Geophys Res: Atmos 2014;119:753–86.
[27] Nousiainen T, Vermeulen K. Comparison of measured single-scattering matrix of feldspar particles with T-matrix simulations using spheroids. J Quant Spectrosc Radiat Transf 2003;79–80:1031–42.
[28] Nousiainen T. Optical modeling of mineral dust particles: a review. J Quant Spectrosc Radiat Transf 2009;110:1261–79.
[29] Kocifaj M, Horvath H, Gangl M. Retrieval of aerosol aspect ratio from optical measurements in Vienna. Atmos Environ 2008;42:2582–92.
[30] Mishchenko MI, Travis LD. Satellite retrieval of aerosol properties over the ocean using polarization as well as intensity of reflected sunlight. J Geophys Res 1997;102:16989–7013.
[31] Kahn R, West R, McDonald D, Rheingans B, Mishchenko MI. Sensitivity of multiangle remote sensing observations to aerosol sphericity. J Geophys Res 1997;102:16861–70.
[32] Kalashnikova OV. Ability of multiangle remote sensing observations to identify and distinguish mineral dust types: optical models and retrievals of optically thick plumes. J Geophys Res 2005;110(D18S4).
[33] Kalashnikova OV, Kahn R. Ability of multiangle remote sensing observations to identify and distinguish mineral dust types: 2. Sensitivity over dark water. J Geophys Res 2006;111:D11207.
[34] Kokhanovsky AA, Leeuw G. Satellite aerosol remote sensing over land. Berlin, Heidelberg: Springer; 2009.
[35] Hasekamp OP, Landgraf J. Retrieval of aerosol properties over land surfaces: capabilities of multiple-viewing-angle intensity and polarization measurements. Appl Opt 2007;46:3332–44.
[36] Dubovik O, Sinyuk A, Lapyonok T, Holben BN, Mishchenko M, Yang P, et al. Application of spheroid models to account for aerosol particle nonsphericity in remote sensing of desert dust. J Geophys Res 2006;111:D11208.
[37] Deuzé JL, Herman M, Goloub P, Tanré D, Marchand A. Characterization of aerosols over ocean from POLDER/ADEOS-1. Geophys Res Lett 1999;26:1421–4.
[38] Goloub P, Tanre D, Deuze JL, Herman M, Marchand A, Breon FM. Validation of the first algorithm applied for deriving the aerosol properties over the ocean using the POLDER/ADEOS measurements. IEEE Trans Geosci Remote Sens 1999;37:1586–96.

[39] Deuzé JL, Goloub P, Herman M, Marchand A, Perry G, Susana S, et al. Estimate of the aerosol properties over the ocean with POLDER. J Geophys Res 2000;105:15329–46.
[40] De Haan J, Bosma P, Hovenier J. The adding method for multiple scattering calculations of polarized light. Astron Astrophys 1987;183:371–91.
[41] Wiscombe WJ. The Delta–M method: rapid yet accurate radiative flux calculations for strongly asymmetric phase functions. J Atmos Sci 1977;34:1408–22.
[42] Hu YX, Wielicki B, Lin B, Gibson G, Tsay SC, Stamnes K, et al. delta-Fit: a fast and accurate treatment of particle scattering phase functions with weighted singular-value decomposition least-squares fitting. J Quant Spectrosc Radiat Transf 2000;65:681–90.
[43] Liou KN, Takano Y, Yang P. Intensity and polarization of dust aerosols over polarized anisotropic surfaces. J Quant Spectrosc Radiat Transf 2013;127:149–57.
[44] Suomalainen J, Hakala T, Puttonen E, Peltoniemi J. Polarised bidirectional reflectance factor measurements from vegetated land surfaces. J Quant Spectrosc Radiat Transf 2009;110:1044–56.
[45] Clough SA, Iacono MJ, Moncet J-L. Line-by-line calculations of atmospheric fluxes and cooling rates: application to water vapor. J Geophys Res 1992;97:15761–85.
[46] Fischer J, Gamache RR, Goldman A, Rothman LS, Perrin A. Total internal partition sums for molecular species in the 2000 edition of the HITRAN database. J Quant Spectrosc Radiat Transf 2003;82:401–12.
[47] Kattawar GW, Plass GN. Asymptotic radiance and polarization in optically thick media: ocean and clouds. Appl Opt 1976;15:3166–78.
[48] Tanré D, Bréon FM, Deuzé JL, Dubovik O, Ducos F, François P, et al. Remote sensing of aerosols by using polarized, directional and spectral measurements within the A-Train: the PARASOL mission. Atmos Meas Tech Discuss 2011;4:2037–69.
[49] C-Labonnote L, Brogniez G, Buriez J-C, Doutriaux-Boucher M, Gayet J-F, Macke A. Polarized light scattering by inhomogeneous hexagonal monocrystals: validation with ADEOS-POLDER measurements. J Geophys Res: Atmos 2001;106:12139–53.
[50] Hsu NC, Tsay SC, King MD, Herman JR. Aerosol properties over bright-reflecting source regions. IEEE Trans Geosci Remote Sens 2004;42:557–69.
[51] Dubovik O, Holben B, Eck TF, Smirnov A, Kaufman YJ, King MD, et al. Variability of absorption and optical properties of key aerosol types observed in worldwide locations. J Atmos Sci 2002;59:590–608.